RJC

RASĀYAN *J. Chem.*
Vol. 18 | No. 4 |1934-1942| October-December | 2025
ISSN: 0974-1496 | e-ISSN: 0976-0083 | CODEN: RJCABP
http://www.rasayanjournal.com
http://www.rasayanjournal.co.in

SYNERGISTIC ENHANCEMENT OF PHOTOCATALYTIC AND ANTI-INFLAMMATORY PROPERTIES IN NICKEL-DOPED ZINC OXIDE NANORODS

J. Princess Gracia[1,✉], V. Nandhakumar[1], J. Prince Richard[2], N. Balasubramanian[3], G. Suganya[1] and V. Bargavi[1]

[1]Department of Chemistry, A.V.V.M. Sri Pushpam College (Affiliated to Bharathidasan University, Tiruchirappalli – 620024), Poondi, Thanjavur, Tamil Nadu, India
[2]ECPS Division, CSIR-CECRI, Karaikudi-630003, Tamil Nadu, India
[3]Department of Chemistry, SRM Institute of Science and Technology, Tiruchirappalli-621105, Tamil Nadu, India
✉Corresponding author: princess.pyr@gmail.com

ABSTRACT

This study successfully produced nickel-infused zinc oxide nanorods through a well-established synthesis via a simple, inexpensive hydrothermal route with different Ni concentrations (0, 1, 3, 5, 7, and 9 wt%). The synthesized nanorods were analyzed to know the structural, optical, and morphological properties using techniques such as SEM, XRD, UV, and PL. Establishment of a well-structured wurtzite formation, and a decrease in crystal size with higher Ni concentrations were confirmed by XRD analysis. Similarly, the optical band gap was found to diminish when the concentration of Ni was increased. The photoluminescence spectra show a red emission peak at 660nm, attributed to oxygen interstitials. The photocatalytic efficiency and inflammation-inhibitory effect of nickel-doped zinc oxide nanorods were assessed. The outcome demonstrates that Ni doping significantly enhances the ZnO nanorods' anti-inflammatory and photocatalytic capabilities.

Keywords: Hydrothermal Method, ZnO Nanorods, Ni, Structural Characteristics, Photoluminescence, SEM, Photocatalytic Activity, and Anti-Inflammatory Properties.

RASĀYAN *J. Chem.*, Vol. 18, No. 4, 2025

INTRODUCTION

As of late, the use of nano-photocatalysts in the removal of contaminants in air and wastewater has drawn the scientists' interest. Photocatalytic water degradation using nanocomposites composed of heterogeneous semiconductors has shown significant potential as an economical and eco-friendly approach for water purification. Since photodegradation occurs when sunshine illuminates a substance, turning harmful pollutants into harmless components, it is evident that this method is more practical than others. The use of nano-semiconductor photocatalysts to cure environmental contamination has sparked growing interest. One-dimensional (1D) photocatalysts are particularly noteworthy among nano-semiconductors due to their exceptional performance. On one hand, they offer a greater surface area in contrast to materials in bulk, providing more contact points during reactions. On the other hand, unlike nanoparticles, after the reactions are finished, it is simpler to filter them out due to their greater aspect ratio. ZnO is a particularly appealing semiconductor photocatalyst among the II–VI subgroup photocatalysts. Because of its non-toxicity, affordability, and environmental friendliness, it is frequently employed for the photodegradation of both organic and inorganic dyes. Snappy carrier recombination is the main factor influencing ZnO's photocatalytic effectiveness. So as to increase its performance, different ions have been doped into ZnO to decrease the photogenerated carrier recombination. Ni's unique combination of steadiness on the Zn lattice makes it stand out among the extremely effective doping materials to improve and customize the properties of ZnO.[1-5] In this present investigation, Zinc oxide nanorods doped with Nickel were created using a cost-effective hydrothermal approach with zinc chloride as precursor, and the influence of nickel incorporation on Zinc oxide nanorods' photocatalytic performance was investigated. In addition, their anti-inflammatory properties were assessed.

Rasayan J. Chem., 18(4), 1934-1942(2025)
http://doi.org/10.31788/RJC.2025.1849399

EXPERIMENTAL

Fabrication of Zinc Oxide Nanorods Doped with Nickel

Zinc oxide nano rods were tailored using zinc chloride ($ZnCl_2$) and nickel chloride hexahydrate as precursors. 4.08g of ZnCl and 0.0408g of $NiCl_2$ $6H_2O$ (1 wt%) mixed in 300ml of deionized water and agitated for 30 minutes at 60° C. A 2 M sodium hydroxide solution is introduced while stirring continuously. The resulting mixture is kept at 90°C in an autoclave for 15 minutes, then the product is filtered, dried thoroughly, and subjected to the heat treatment for three hours at 250°C in a muffle furnace to produce powdered Ni-doped Zinc oxide nanorods. The same procedure was systematically applied for varying weight percentages of Ni concentration (3, 5, 7, and 9 wt.%).

Photodegradation Experiment for Methyl Violet Dye

The methyl violet dye was subjected to photodegradation, having the nanorods under sunlight illumination, for the assessment synthesized nickel-doped zinc oxide nanorods for their photo-induced catalytic efficiency. A sunny day was chosen to carry out the above experiment. The following was the photocatalysis experimental setup: 100 mL of an aqueous methyl violet (MV) solution containing 10 mg/L was used to disperse 0.03 g of Ni-doped ZnO, abbreviated as Ni/ZnO nanorods. The solution was agitated without illumination for half an hour to achieve equilibrium between the Ni/ZnO nanorods and the dye molecules. Aliquots were then taken at 15-minute intervals (up to 90 minutes), keeping the suspension in sunlight. The catalyst was rapidly isolated from the reaction mixture through centrifugal separation. The deterioration of the dye shifted the suspension's color from dark violet to pale violet, to progressively shifted and finally to colorless. The quantification of inclusion of MV dye in the test specimens was ascertained employing a UV-Visible spectrophotometric analysis.

Anti-Inflammatory Assessment

The anti-inflammatory activity of synthesized zinc oxide nanorods doped with varying nickel concentrations (1, 3, 5, 7, and 9 wt.%) was assessed through the BSA denaturation method. The commercial reference medication Diclofenac Sodium and test samples were first dissolved in 1 mL of 2.5% dimethylformamide (DMF), then diluted with 0.2 M phosphate in order to keep their pH values at 7.0. A 1 mL aliquot of the test solution, containing varying concentrations of nanoparticles (15 to 240 µg/mL), was incubated at 27 °C for 10 minutes in a water bath. The % inhibition of protein denaturation was computed by spectrophotometrically measuring the solution's turbidity at 660 nm.

$$Percentage\ Inhibition = \frac{Abs\ Control - Abs\ Sample}{Abs\ Control} x100$$

Characterization Tools

The phase composition and crystal structure and ZnO nanorods doped with different Ni concentrations ranging from 0 to 9 (weight percent) were examined using the X-ray diffraction technique with the SHIMADZU-XRD 6000 system. Morphological features were analysed using Hitachi S-4500 SEM. A SHIMADZU-UV 1800 spectrophotometer was used for recording the optical absorptions. The PL spectrum, excited at 300 nm and measured at ambient temperature, was obtained using a VARIAN fluorescence spectrophotometer.

Findings and Analysis

Crystallographic Characterization

Figure-1 represents the XRD spectra of Zinc oxide nanorods with varying Ni concentrations and pure Zinc oxide nanorods. All reveal a distinct crystalline hexagonal wurtzite phase, according to the JCPDS card: 36-1451. The observed peaks correspond to planes of (100), (002) (101), (102), (110), (103), (200), (112), (201), and (202), respectively. No other impurity peaks of Ni or its oxides were found up to a doping concentration of 6 wt%. When Ni concentration increases above 6 wt.%, the sample shows secondary phase (NiO) related peaks with minimal intensity. This means that at above 6 wt.%, the Ni content reaches its solubility limit.[6,7] Figure-2 illustrates the 2θ shift of the peak with maximum intensity. In Fig.-2, with greater Ni doping levels, a shift to higher angles is observed. This shift, along with the reduction in peak intensity, provides evidence for the incorporation of Ni^{2+} ions into the ZnO lattice.[8]

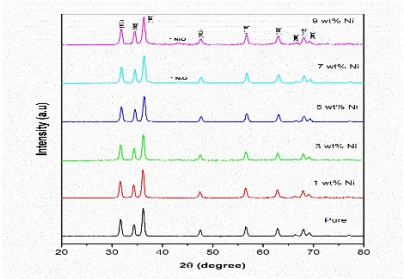

Fig.-1: X-ray Diffraction Spectra of Ni-doped ZnO Synthesized at different Ni Concentrations (0, 1, 3, 5, 7, and 9 wt.%)

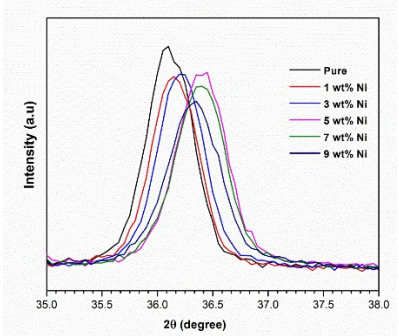

Fig.-2: 2θ Shift of the Prominent Peaks

Table-1: Microstructural Parameters of Ni-doped ZnO Synthesized at Different Ni Concentrations (0, 1, 3, 5, 7, and 9 wt%)

Sample (wt%)	Crystallite size D (nm)	Dislocation Density $\delta \times 10^{14}$ lines/m^2	Micro strain ε	Stacking Fault (SF)
Pure	27.19	13.5264	0.00136	0.00237
1	26.54	14.1971	0.00138	0.00246
3	26.13	14.6461	0.00141	0.00251
5	25.42	15.4757	0.00143	0.00262
7	25.92	14.8844	0.00139	0.00258
9	26.33	13.5264	0.00137	0.00237

Crystal domain size was determined using Scherrer's equation from the 2θ values and the FWHM of the (hkl) peaks. Structural parameters, including microstrain (ε), dislocation density (δ), and stacking faults (SF), are listed in Table-1. At the same time, atomic packing fraction (APF), lattice constants' 'a and 'c, and unit cell volume are presented in Table-2. With increasing Ni concentration, a reduction in crystallite size was observed, particularly in the (101) peak, attributed to lattice distortion from Ni doping.

Table-2: Lattice Constants, Atomic Packing Fraction, and Unit Cell Volume of Ni-doped ZnO Synthesized at different Ni concentrations (0, 1, 3, 5, 7, and 9 wt.%)

Sample (wt%)	Lattice Constant (Å)		Atomic Packing Fraction(%)	Unit Cell Volume (Å^3)
	a	C		
Pure	3.274	5.274	75.58	48.68
1	3.269	5.271	75.61	48.65
3	3.263	5.265	75.63	48.61
5	3.258	5.261	75.67	48.58
7	3.261	5.264	75.64	48.63
9	3.266	5.268	75.59	48.67

This distortion limits nucleation and growth, and the data show a decrease in APF, lattice constants, and unit cell volume, consistent with the smaller ionic radius of Ni^{2+} compared to Zn^{2+}. The shift in 2θ and contraction of lattice parameters further confirm the substitution of Zn^{2+} by Ni^{2+} in the ZnO lattice.[9,10]

Optical Studies

The contribution of nickel to the photonic features of the synthesized ZnO nanorods was examined using UV-Visible spectroscopy. Figure-3 illustrates the absorption spectra of ZnO nanorods incorporated with varying concentrations of nickel (0, 1, 3, 5, 7, and 9 wt%). At 329 and 375 nm, two absorption peaks were discovered. The ld-electrons of Ni ions, which occupied the place of the cations inside the structure, interact with the band electrons of the ZnO lattice to produce this effect. Figure-4 represents the $(\alpha h\nu)^2$ vs. hν plot for the synthesized ZnO nanorods. The linear portion of the curve was extended until it intersected the hv axis in order to determine the band gap values. The estimated' band gap' energies for varying Ni concentrations (0, 1, 3, 5, 7, and 9 wt.%) are 3.260eV, 3.252eV, 3.222eV, 3.186eV, 3.212eV, and 3.243eV. It has been found that the bandgap values exhibit a declining trend with increasing Ni concentration, reaching a minimum at 6 wt.%. The limited d-electrons of Ni cause interaction with the band electrons of the ZnO lattice, which decreases the band gap. The band gap value increases when the Ni concentration is above 6 wt.%, owing to the generation of secondary phase NiO, which has a wide bandgap.[11-14]

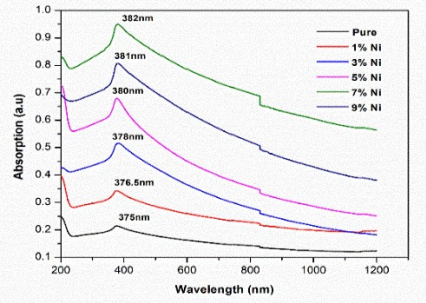

Fig.-3: Absorption Spectra of Ni-doped ZnO Synthesized at different Ni Concentrations (0, 1, 3, 5, 7, and 9 wt.%)

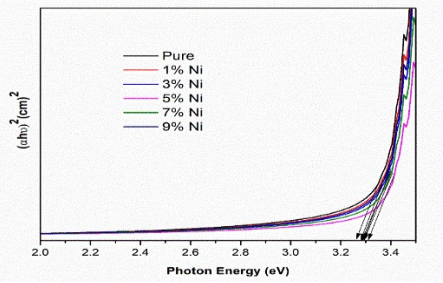

Fig.-4: Bandgap Energy Calculation of Ni-doped ZnO Nanorods

Morphological Analysis

Figure-5 portrays the SEM image of ZnO nanorods fabricated at different Ni concentrations (0, 1, 3, 5, 7, and 9 wt.%). From the image, it has been found that with the increase of Ni concentrations up to 5 wt.%, the ZnO nanorods attain regular morphology with increased length the decreased diameter. With further increase in Ni concentrations, the image shows irregularly shaped agglomerated particles. The secondary phase's creation is the cause of this event.

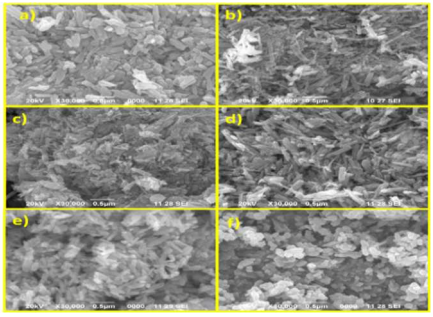

Fig.-5: Scanning Electron Microscope images of Pure and Ni-doped ZnO Nanorods at different Ni Concentrations(a) Pure (b) 1 wt.% Ni (c) 3 wt.% Ni (d) 5 wt.% Ni (e) 7 wt.% Ni (f) 9 wt..% Ni

The EDAX spectra of zinc oxide nanorods doped with nickel at different concentrations (0, 1, 3, 5, 7, and 9 weight percent) are shown in Fig.-6. Table-3 shows the wt% of Zinc, Oxygen, and Nickel in the Ni-doped ZnO nanorods synthesized at varying Ni concentrations (0, 1, 3, 5, 7, and 9 wt.%). It is clear that with increasing doping percentage, the wt% of Ni in the samples increases.

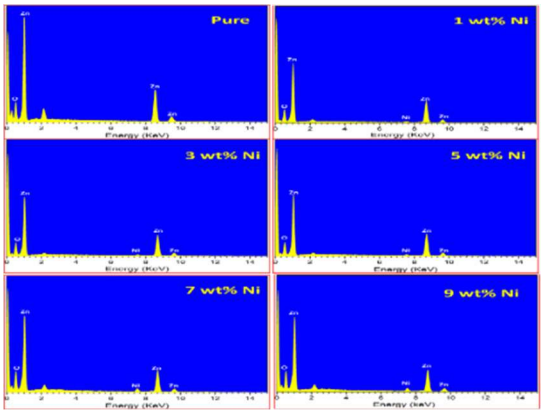

Fig.-6: EDAX Spectrum of Pure and Ni-doped ZnO Nanorods at different Ni Concentrations

Table-3: Compositional Analysis of Ni-incorporated ZnO Synthesized at Varying Doping Levels (0, 1, 3, 5, 7, and 9 wt%).

Sample (wt%)	Elements	Weight %
Pure	Zn	70.99
	Ni	0
	O	29.01
1	Zn	70.05
	Ni	0.86
	O	29.09
3	Zn	69.07
	Ni	1.21
	O	29.72
5	Zn	68.11
	Ni	2.96
	O	28.93
7	Zn	65.33
	Ni	5.02
	O	29.65
9	Zn	63.47
	Ni	7.31
	O	29.22

Photoluminescence Study

Figure-7 presents the steady-state PL spectra at room temperature of the nickel-doped Zinc oxide nanorods produced with varying amounts of Ni (0, 1, 3, 5, 7, and 9 wt%) estimated over a wavelength range of 400-750nm. As found in Fig.-7, two separate emission bands are visible in zinc oxide nanorodswhich are a strong emission at 660 nm(red region) and a weak emission at 430 nm (blue region). The 430 nm peak, being relatively weak, indicates the near-band-edge emission characteristic of ZnO, attributed to excitonic recombination driven by interactions between excitons. The presence of extra oxygen, mostly in the form of oxygen interstitials, is responsible for the main red emission peak at 660 nm. A gradual reduction in the red emission peak intensity is noted with increasing Ni concentration up to 5 wt%, primarily due to a decrease in oxygen vacancy defects. Ni doping prevents oxygen vacancies from forming. The insertion of transition metal ions into Zinc Oxide speeds up non-radiative decay processes, which explains the red emission peak's decreased intensity. Ni^{2+} dopants act as electron traps, suppressing the recombination of charge carriers. An additional increase in Ni concentration leads to a rise in red emission intensity, mostly as a result of NiO's secondary phase development.[15,16]

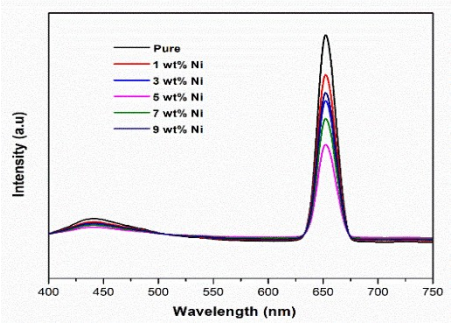

Fig.-7: PL Spectra of Ni Doped ZnO Synthesized at different Ni Concentrations (0, 1, 3, 5, 7, and 9 wt%)

Assessment of Photocatalytic Efficiency

The efficiency of photocatalysis of nickel-doped Zinc oxide nanorods produced with varying Ni concentrations (0, 1, 3, 5, 7, and 9 weight percent) was evaluated by monitoring the Methyl Violet dye's deterioration under solar radiation. Upon absorption of supra-bandgap photons, electron-hole pairs are generated within the semiconductor particles, thereby triggering the photocatalytic reaction. Following their diffusion to the particle surface, the charge carriers react with the water molecules, which produce superoxide (O_2^-) and hydroxyl radicals, which are extremely reactive and aid in the deterioration of adsorbed organic materials.[17,18] The deterioration mechanism is elucidated as follows:

$$Ni/ZnO + h\upsilon \rightarrow e_{CB}^- + h_{VB}^+$$

Oxygen species adsorption

$$O_2 + e_{CB}^- \rightarrow O_2^*$$

Conversion of the hydroxyl moiety (OH) into hydroxyl radicals (OH) by photogenerated holes

$$H_2O + h_{VB}^+ \rightarrow H^* + OH^*$$

$$O_2^* + OH^* + \text{Methyl Violet} \rightarrow CO_2 + H_2O \text{ (Degradation Products)}$$

The percentage of MV dye degradation (%D) is obtained through the equation given below,

$$\%D = \frac{C_0 - C_t}{C_0} X\ 100$$

Where C_0 signifies the dye concentration at the initial stage, whereas C_t indicates the dye concentration following specified periods (0–90 min) of irradiation exposure. Figure-8 depicts the range of absorption of MV dye subjected to degradation by Ni-doped ZnO nanorods with varying Ni concentrations (0, 1, 3, 5, 7, and 9 weight percent) at 0, 15, 30, 45, 60, 75, and 90-minute intervals. The reduction in MV concentration was determined by observing changes in the magnitude of the absorption peak at 583 nm. From the Fig.-8 it is clear that with prolonged irradiation, the MV absorption peak's strength steadily decreases.

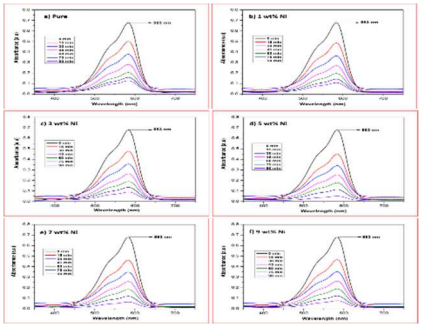

Fig.-8: Time-dependent UV-Vis Absorption Spectra of MV under Irradiation in the Presence of Ni-doped ZnO Photocatalyst

The effect of the contact duration (0–90 min) of the synthesized zinc oxide catalyst produced at various Nickel dosages (0, 1, 3, 5, 7, and 9 wt.%) on the degradation percentage of MV dye was examined. The findings, as detailed in Table-4, indicate that the degradation efficiency of MV dye increases with rising

Ni concentration, attaining a maximum at 5 wt.%. This occurs as a result of the doped Ni^{2+} trapping electron and hole recombination, which triggers the photodegradation process. The decline in MV dye degradation efficiency at higher Ni concentrations stems from the formation of a secondary NiO phase, which hinders the catalytic activity. The optimal degradation efficiency of MV dye, measured at 92.51%, was reached within 90 minutes of sunlight exposure with 5 wt.% Ni-doped ZnO nanorods.

Table-4: Degradation of MV dye by Ni-doped ZnO Nanorods

Time (min)	% Degradation of MV Dye					
	Pure	1 wt% Ni	3 wt% Ni	5 wt% Ni	7 wt% Ni	9 wt% Ni
0	0	0	0	0	0	0
15	26.13	28.34	29.82	33.5	32.04	31.30
30	44.25	46.48	47.59	49.82	48.71	48.15
45	58.51	60.17	61.41	62.66	61.83	61.41
60	69.89	71.09	72.00	73.80	72.90	72.30
75	76.74	79.07	80.23	83.25	82.55	82.09
90	81.30	84.10	86.91	92.51	90.64	88.69

Kinetic Evaluation

It is known that organic dye degradation under photocatalytic conditions usually proceeds according to pseudo-first-order kinetics:[19-21]

$$\ln(C_0/C_t) = kKt = kt \quad \text{or} \quad C_t = C_0\, e^{-kt}$$

Table-5: Kinetic Rate Constant and Correlation Coefficient for MV Dye Degradation

Sample (wt%)	Rate Constant	Correlation Coefficient (R^2)
Pure	0.0189	0.9978
1	0.0235	0.9920
3	0.0220	0.9975
5	0.0205	0.9996
7	0.0281	0.9895
9	0.0249	0.9813

Figure-9 presents the results of the photo-induced degradation study of MV dye interacting with ZnO nanorods doped with nickel. The rate constant (k) for MV dye destruction is aided by ZnO nanorods doped with Ni, was calculated by employing the pseudo-first-order kinetic model. The rate constant and correlation coefficient (R^2) are obtained from the relationship between $\ln(C_0/C_t)$ and irradiation time; Table 5 provides specifics of the findings.

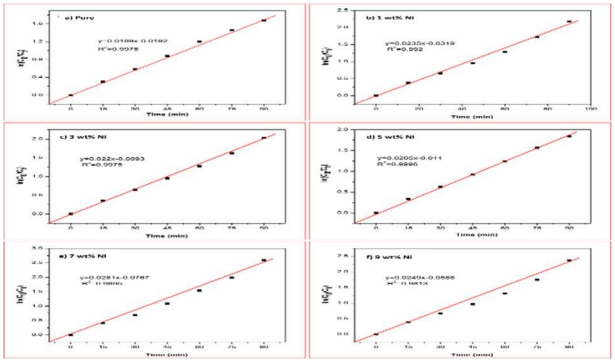

Fig.-9: Relation Curve between $\ln(C_0/C_t)$ and Time (t)

Anti-Inflammatory Property

The anti-inflammatory effectiveness of the ZnO nanorods doped with Ni, synthesized at different Ni concentrations (0, 1, 3, 5, 7, and 9 weight percent) using the BSA denaturation technique, with findings outlined in Table-6, was employed for the analysis.

The results show that Ni-doped ZnO nanorods exhibit improved anti-inflammatory performance compared to Diclofenac sodium, a standard anti-inflammatory agent. This is because Ni doping into ZnO modifies its electronic and structural features, resulting in enhanced stabilization of BSA and suppression

of protein denaturation. The enhanced anti-inflammatory activity of Ni-doped ZnO over undoped ZnO is attributed to a synergy of enhanced surface reactivity, increased ROS generation, changes in electronic properties, and enhanced biocompatibility. These combined to make Ni-doped ZnO a more viable agent in the treatment of inflammation.[22]

Table-6: Anti-Inflammatory Efficiency of Ni-doped ZnO Nanorods

Different concentration (µg/ml)	Percentage inhibition (%)						
	Standard (Diclofenac sodium)	Pure	1 wt% Ni	3 wt% Ni	5 wt% Ni	7 wt% Ni	9 wt% Ni
15	15.04±0.45	22.80±0.04	23.40±0.11	25.11±0.3	27.90±0.08	26.31±0.11	25.76±0.14
30	26.91±0.14	27.12±0.67	28.32±0.14	29.41±0.03	33.52±0.17	32.14±0.05	30.12±0.16
60	29.47±0.16	31.45±0.31	33.21±0.21	35.15±0.28	38.14±0.41	37.04±0.32	36.05±0.11
120	47.19±0.22	51.84±0.86	54.13±0.16	55.21±0.43	58.14±0.06	56.14±0.16	55.84±0.22
240	75.17±0.16	87.44±0.81	89.13±0.31	91.54±0.43	95.21±0.32	93.55±0.41	92.62±0.08

CONCLUSION

Nickel-doped zinc oxide nanorods were produced using an uncomplicated synthesis approach, a cost-effective hydrothermal route. From XRD analysis, it has been found that the nanorods exhibit a well-crystallized wurtzite structure, and the crystal size is found to shrink when the doping concentration exceeds 5 weight percent. Ni^{2+} ions' smaller ionic radius contributes to the initial reduction in crystal size, but an excessive Ni concentration induces the formation of a secondary NiO phase, ultimately resulting in crystal growth. SEM imaging substantiates the formation of nanorods with a well-ordered morphology. Notably, the replacement of Zn^{2+} ions within the ZnO lattice by Ni^{2+} is responsible for the decreasing trend in the optical band gaps of the nanorods as the quantity of Ni rises. A well-defined red emission peak at 660 nm is prominently featured in the PL spectra. The presence of Ni^{2+} ions restricts charge carrier recombination, which is a key factor in the photodegradation process. Using Methyl Violet dye as a typical pollutant, Ni-doped ZnO nanorods' photocatalytic ability was assessed. The observations confirm that ZnO nanorods with 5 wt% Ni exhibit exceptional photocatalytic efficiency. The results clearly show that adding Ni to the ZnO lattice maximizes its photocatalytic activity, making it an effective material for breaking down organic dyes. The anti-inflammatory efficiency of ZnO nanorods was analysed using the Bovine serum albumin denaturation method. The addition of Nickel (Ni) to ZnO enhances its anti-inflammatory ability via the modification of its structural, optical, and electronic characteristics. Ni doping causes defect states, increases charge separation, and elevates surface reactivity, therefore leading to enhanced biomolecular interaction like that of Bovine Serum Albumin (BSA). This improves the stabilization of the protein and prevents denaturation, a significant role to play in the reduction of inflammation. Ni doping also increases the antioxidant nature of ZnO, further increasing its anti-inflammatory properties.

ACKNOWLEDGMENTS

The authors are grateful to those who offered suggestions when they were writing this work.

CONFLICT OF INTERESTS

The authors declare that there is no conflict of interest.

AUTHOR CONTRIBUTIONS

The present work is related to *SDG-3: Good Health and Well-being*. All the authors contributed significantly to this manuscript, participated in reviewing/editing and approved the final draft for publication. The research profile of the authors can be verified from their ORCID ids, given below:

J. Princess Gracia http://orcid.org/0000-0001-8744-4867
V. Nandhakumar http://orcid.org/0000-0003-2186-7239
J. Prince Richard http://orcid.org/0000-0002-9783-0531
N. Balasubramanian http://orcid.org/0009-0008-7097-4130
G. Suganya http://orcid.org/0009-0009-6963-1111
V. Bargavi http://orcid.org/0009-0000-8222-358X

REFERENCES

1. K. Raja, P.S Ramesh and D. Geetha, *Spectrochimica Acta Part A: Molecular and Biomolecular Spectroscopy*, **120**, 19(2014), https://doi.org/10.1016/j.saa.2013.09.103
2. J. Zhao, L. Wang, X. Yan, Y. Yang, Y. Lei, J. Zhou, Y. Huang, Y. Gu and Y. Zhang, *Materials Research Bulletin*, **46(8)**,1207(2011), https://doi.org/10.1016/j.materresbull.2011.04.008
3. R. Philipus, A. Noorhidayati, N. F. Djaja and R. Saleh, *Materials Science Forum*, **827**, 25(2015), https://doi.org/10.4028/www.scientific.net/MSF.827.25
4. N. V. Kaneva, D. T. Dimitrov and C. D. Dushkin, *Applied Surface Science*, **257(18)**,8113(2011), https://doi.org/10.1016/j.apsusc.2011.04.119
5. I. Ahmad, M. Aslam, U. Jabeen, M. N. Zafar, M. N. K. Malghani, N. Alwadai, F. H. Alshammari, A. S. Almuslem and Z. Ullah, Inorganica Chimica Acta, **543,** 121167(2022), https://doi.org/10.1016/j.ica.2022.121167
6. B. Pal, D. Sarkar and P. K. Giri, *Applied Surface Science*, **356**, 804(2015), https://doi.org/10.1016/j.apsusc.2015.08.163
7. R. Chauhan, A. Kumar and R. P. Chaudhary, *Research on Chemical Intermediates*, **38**, 1483(2012), https://doi.org/10.1007/s11164-011-0478-5
8. J.K. Salem, T. M. Hammad and R. R. Harrison, *Journal of Materials Science: Materials in Electronics*, **24**, 1670(2013), https://doi.org/10.1007/s10854-012-0994-0
9. J. P. Richard, I. K. Punithavathy, S. J. Jeyakumar, M. Jothibas and P. Praveen, *Journal of Materials Science: Materials in Electronics*, **28**, 4025(2017), https://doi.org/10.1007/s10854-016-6016-x
10. I.K. Punithavathy, J. P. Richard, S. J. Jeyakumar, M. Jothibas and P. Praveen, *Journal of Materials Science: Materials in Electronics*, **28**, 2494(2017), https://doi.org/10.1007/s10854-016-5823-4
11. T. Jan, J. Iqbal, M. Ismail, Q. Mansoor, A. Mahmood, and A. Ahmad, *Applied Surface Science*, **308**, 75(2014), https://doi.org/10.1016/j.apsusc.2014.04.100
12. S. C. Das, R. J. Green, J. Podder, T. J. Regier, G. S. Chang and A. Moewes, *The Journal of Physical Chemistry C*, **117(24)**,12745(2013), https://doi.org/10.1021/jp3126329
13. J. Mohapatra, D. K. Mishra, S. K. Kamilla, V. R. R. Medicherla, D. M. Phase, V. Berma and D. K. Singh, *Physica Status Solidi B,* **248(6)**, 1352(2011), https://doi.org/10.1002/pssb.201046513
14. P. V. Radovanovic and D. R. Gamelin, *Physical Review Letters,* **95***,* 157202(2003), https://doi.org/10.1103/PhysRevLett.91.157202
15. D. Guruvammal, S. Selvaraj and S. Sundar, *Journal of Alloys and Compounds,* **682**, 850(2016), https://doi.org/10.1016/j.jallcom.2016.05.0388
16. K. P. Shinde, R. C. Pawar, B. B. Sinha, H. S. Kim, S. S. Oh and K.C. Chung, *Ceramics International.* **40(10)**,16799(2014), https://doi.org/10.1016/j.ceramint.2014.07.148
17. K. Jeyasubramanian, G S, Hikku and R. K. Sharma, *Journal of Water Process Engineering,* **8**, 35(2015), https://doi.org/10.1016/j.jwpe.2015.08.007
18. M. H. Baek, J. W. Yoon, J. S. Hong and J. K. Suh, *Applied Catalysis A: General*, **450**, 222(2013), https://doi.org/10.1016/j.apcata.2012.10.018
19. X. Chang, Z. Li, X. Zhai, S. Sun, D. Gu, L. Dong, Y. Yin and Y. Zhu, *Materials & Design,* **98**, 324(2016), https://doi.org/10.1016/j.matdes.2016.03.027
20. H. A. Le, L. T. Linh, S. Chin and J. Jurng, *Powder Technology,* **225**, 167(2012), https://doi.org/10.1016/j.powtec.2012.04.004
21. M. Jothibas, C. Manoharan, S. J. Jeyakumar, P. Praveen, I. K. Punithavathy and J. P. Richard, *Solar Energy,* **159**. 434(2018), https://doi.org/10.1016/j.solener.2017.10.055
22. P.C. Nagajyothi, S. J. Cha, I. J. Yang, T.V.M. Sreekanth, K. J. Kim and H. M. Shin, *Journal of Photochemistry and Photobiology B: Biology*, **146**, 10(2015), https://doi.org/10.1016/j.jphotobiol.2015.02.008

[RJC-9399/2025]